Letter Vol. 49, No. 1 / 1 January 2024 / Optics Letters 49

Laser-written wave plates inside the silicon enabled by stress-induced birefringence

Alperen Saltik[1] and Onur Tokel[1,2,*]

[1]Department of Physics, Bilkent University, Ankara 06800, Turkey
[2]UNAM – National Nanotechnology Research Center and Institute of Materials Science and Nanotechnology, Bilkent University, Ankara 06800, Turkey
*otokel@bilkent.edu.tr

Received 29 August 2023; revised 21 November 2023; accepted 21 November 2023; posted 21 November 2023; published 19 December 2023

Laser writing enables optical functionality by altering the optical properties of materials. To achieve this goal, efforts generally focus on laser-written regions. It has also been shown that birefringence surrounding the modified regions can be exploited for achieving functionality. The effect has been used to fabricate wave plates in glass, with significant potential for other materials. Here, we establish analogous stress control and birefringence engineering inside silicon. We first develop a robust analytical model enabling the prediction of birefringence maps from arbitrary laser-written patterns. Then, we tailor three-dimensional laser lithography to create the first, to the best of our knowledge, polarization-control optics inside silicon.

https://doi.org/10.1364/OL.504600

Polarization degree-of-freedom plays a critical role in numerous areas of science and technology [1]. Thus, there is significant interest towards on-demand polarization control for diverse design considerations [2]. In particular, plug-and-play free-space polarization optics, which could be rapidly fabricated and deployed, is strongly desired [3]. Direct laser writing is emerging as a rapid and inexpensive paradigm for fabricating state-of-the-art optical devices [4,5]. In these techniques, the laser is focused in a transparent material, inducing nonlinear processes to create controlled modifications, leading to three-dimensional (3D) modulation of optical properties [6]. The precise control in 3D enables significant advances in the fabrication of optical elements, e.g., with ultrafast-laser-structuring inside glasses [7–11]. Through modulating optical properties on or around laser-written areas, polarization control and wave plate creation are achieved for the visible regime [9–11]. Fabricating such wave plates in the infrared is also possible, however challenging [9], due to potential transmission losses.

Here, we consider silicon (Si), due to its high infrared transparency, as well as its significant integration potential as the backbone of electronics, electro-optics, photovoltaics, and Si-photonics industries. The 3D nonlinear laser lithography of Si is emerging as a powerful paradigm to exert optical control deep inside the wafer, without altering the wafer surface [4]. The subsurface lithography efforts in Si are already enabling various amplitude- and phase-control optics, including waveguides and holograms [4,12–15]. In contrast, polarization control inside Si is lacking. Motivated by the preceding considerations, we aim to develop a general framework for stress-induced birefringence control in Si. We first observe that the stress surrounding the laser-written structures in Si can create birefringence due to stress-optical effects, analogous to glass [16–18]. By analyzing experimental retardance from basic structures, we develop an analytical model that directly connects laser-written patterns to retardance maps. The model provides insight into birefringence of diverse laser-written patterns. Then, guided by this model, we tailored the laser lithography parameters and the 3D architecture in order to create quarter-wave plates (QWPs) and half-wave plates (HWPs) inside Si.

Our model is based on cylindrical structures forming the basic building units. In the selected laser lithography regime for this Letter, the laser irradiation creates cylindrical structures of the radius ~ 3 μm over a plane formed by the x and y coordinates, with an elongation of ~ 100 μm along the z coordinate (Fig. 1). Thus, we consider a two-dimensional (2D) model with plane-strain conditions, i.e., no z dependency. We consider the laser-written structure as a "pressurized hole" (PH) and use the associated stress tensor of the PH model [19]. The compressive stress exerted by such a structure is illustrated in Fig. 1(a).

The Cauchy stress tensor for the associated PH model in polar coordinates is given as (see Supplement 1, section 1) [19]:

$$\boldsymbol{\sigma}_{r,\theta} = \begin{bmatrix} \sigma_r = \dfrac{\alpha}{r^2} & \sigma_{r\theta} = 0 \\ \sigma_{\theta r} = 0 & \sigma_\theta = -\dfrac{\alpha}{r^2} \end{bmatrix}. \tag{1}$$

Here, α relates to the magnitude and direction of the radial stress, and r and θ are the polar coordinates. The principal stress directions which diagonalize $\boldsymbol{\sigma}_{r,\theta}$ in Eq. (1) are $\hat{r}$ and $\hat{\theta}$ (see Supplement 1). This enables us to write the photoelastic equation for isotropic materials, as well as for some anisotropic materials including Si (see Supplement 1) as:

$$n_r - n_\theta = C(\theta)(\sigma_r - \sigma_\theta) = C(\theta)\frac{2\alpha}{r^2}, \tag{2}$$

where n_r, n_θ are refractive indices along the principal axes and $C(\theta)$ is a material-dependent photoelastic constant. $C(\theta)$ is constant for isotropic materials, whereas it can be decomposed into harmonic functions of θ for Si (see Supplement 1).

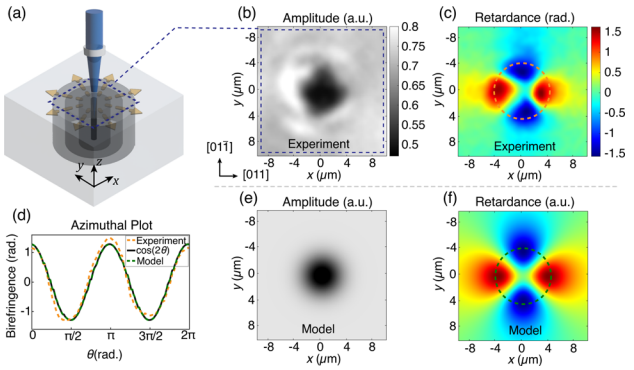

Fig. 1. Compressive stress resulting from a simple laser-written structure on its surroundings is shown in (a), with the associated transmission microscope image in (b) and experimental retardance map in (c). The orange contour in (c) and the green contour in (f) are plotted in (d), along with the cos(2θ) function. The computational model of the basic micro-structure is shown in (e), along with the associated retardance map in (f), evaluated with the developed model.

Then, the Jones matrix associated with the PH model can be written in polar coordinates as:

$$\mathbf{T} \equiv e^{i2\pi n_\theta d/\lambda} \begin{bmatrix} e^{i\Delta\varphi} & 0 \\ 0 & 1 \end{bmatrix}_{r,\theta}. \tag{3}$$

Here, $\Delta\varphi$ is the phase difference acquired by the radial and azimuthal polarizations, given as:

$$\Delta\varphi = \frac{2\pi d}{\lambda}(n_r - n_\theta) = \frac{2\pi d}{\lambda} C(\theta) \frac{2\alpha}{r^2}, \tag{4}$$

Applying coordinate transformations, $\mathbf{T}$ can also be written in the Cartesian coordinates basis as (see Supplement 1):

$$\mathbf{T} \equiv \begin{bmatrix} e^{i\Delta\varphi}\cos^2(\theta) + \sin^2(\theta) & (e^{i\Delta\varphi} - 1)\sin(\theta)\cos(\theta) \\ (e^{i\Delta\varphi} - 1)\sin(\theta)\cos(\theta) & e^{i\Delta\varphi}\sin^2(\theta) + \cos^2(\theta) \end{bmatrix}_{x,y}. \tag{5}$$

Interferometric phase imaging with $\hat{x}$- and $\hat{y}$-polarized light allows extraction of diagonal elements of $\mathbf{T}$ ($\mathbf{T}_{11}$ and $\mathbf{T}_{22}$). These can be used to map the retardance between the $\hat{x}$ and $\hat{y}$ directions, given as $\mathcal{B}_0$ (See Supplement 1):

$$\mathcal{B}_0 = \varphi_y - \varphi_x = \arg(\mathbf{T}_{22}) - \arg(\mathbf{T}_{11}). \tag{6}$$

We aim to find the simplest function that describes salient features of the retardance induced by laser writing. In our analysis detailed in Supplement 1, section 1, we observe that for isotropic materials, as well as for Si, $\mathcal{B}_0$ can be approximated with the following simple form, in particular for large r:

$$\mathcal{B}_0(r,\theta) = \beta r^{-2}\cos(2\theta), \tag{7}$$

where β is a proportionality constant. As we are only interested in the region $r>r_0$, we ignore the singularity at $r = 0$. The solutions for $r<r_0$ can also be analyzed, and a full-field solution may be developed by regarding boundary conditions; however, it is beyond the scope of this Letter. The $\mathcal{B}_0$ function can be written in Cartesian coordinates as:

$$\mathcal{B}_0(x,y) = \beta\left(x^2+y^2\right)^{-1}\cos\left(2\tan^{-1}\left(\frac{y}{x}\right)\right). \tag{8}$$

We recall that $\mathcal{B}_0(x,y)$ describes the retardance caused by a low-diameter, cylindrically symmetric unit. Then, we consider an extended laser-written pattern denoted as LW(x,y), which can take values between 0 and 1, where 0 (1) denotes pristine (laser modified) material. The retardance due to this general laser-written pattern can be generated as the spatial superposition of $\mathcal{B}_0(x',y')$ functions, centered at different locations $(x',\ y')$, by exploiting the linearity of the stress tensors [19]. This process can be written as a two-dimensional convolution:

$$\mathcal{B}(x,y) = \mathrm{LW}(x,y) \circledast \mathcal{B}_0(x,y). \tag{9}$$

LW(x,y) is the function describing the laser-written geometry, and $\mathcal{B}_0(x,y)$ term is the transfer function associating the written pattern (LW(x,y)) to the retardance map ($\mathcal{B}(x,y)$). The only unknown parameter in this relation is the scaling parameter β from Eq. (8), which is to be determined from experiments. We note that Eq. (9) can be expressed as multiplication in the Fourier domain using the convolution theorem:

$$\mathcal{B}(x,y) = \mathrm{FT}^{-1}\left[\mathrm{FT}\left[\mathrm{LW}(x,y)\right].\mathrm{FT}\left[\mathcal{B}_0(x,y)\right]\right]. \tag{10}$$

This allows rapid calculation of retardance patterns from complex laser-written areas using the Fast Fourier Transform (FFT).

In order to test our model, we start by evaluating the basic cylindrically symmetric structure illustrated in Fig. 1(a). The laser writing is performed with a custom-built nanosecond laser ($\sim$ 10 ns), centered at λ = 1.55 μm, with 2 μJ pulse energy and 150 kHz repetition rate, and is set to circular polarization (see Supplement 1, sections 2 and 3) [4]. The beam is focused directly inside Si, irradiating the sample for 3 s. The microscope image of the fabricated structure is shown in Fig. 1(b), with the measured retardance map given in Fig. 1(c). The retardance analysis is performed with a home-built interferometric phase microscope, using a continuous-wave laser of λ = 1.058 μm (see Supplement 1, section 4). The two phase images from the microscope are recorded with orthogonal polarizations (along the y and x axes), where their difference is used to evaluate the final retardance map. For simplicity, we approximated the micro-structure with a Gaussian profile of width equal to the experimental structure (Fig. 1(e)). Then, this geometry is convolved with the transfer function using Eq. (10), producing the retardance map Fig. 1(f). Comparing Figs. 1(c) and 1(f), we observe that the model fairly closely predicts the retardance around the basic laser-written geometry.

The versatility of the model may be checked by two further considerations: (i) its predictive capability for general patterns, and (ii) its potential for enabling novel stress-based optics. In order to evaluate the former, we generate a complicated laser-written shape and compare its measured retardance map with the prediction of our model. A five-pointed star pattern is created inside Si (Fig. 2(a)), and then the associated retardance map is acquired with interferometric phase microscopy (Fig. 2(c)). Our analysis suggests that this map can, in principle, be estimated by the convolution of laser-written geometry (Fig. 2(a)) with the unknown transfer function (Fig. 2(b)). We computationally replicate the star pattern (Fig. 2(d)) and then operate it with the estimated transfer function in our model (Fig. 2(e)). The resulting retardance map is shown in Fig. 2(f).

The striking similarity between Figs. 2(c) and 2(f) satisfies the first consideration given above. The minor differences are likely caused by fabrication and imaging artifacts, as well as the assumption of z-independence (pressurized hole model). We further observe that even though our method focuses only

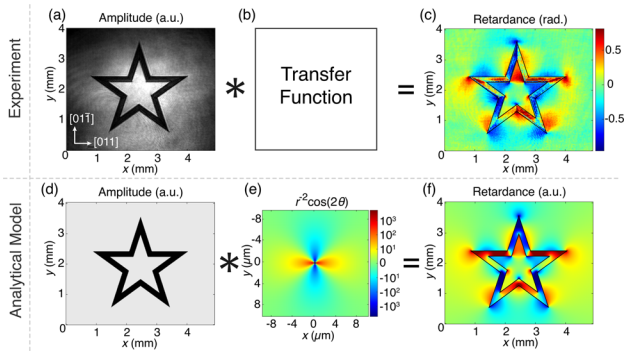

Fig. 2. (a) Transmission microscope image of a laser-written star pattern. (b) Unknown transfer function from written pattern to retardance. (c) Experimental retardance map. (d) Computational recreation of the star shape. (e) Transfer function in our model. (f) Predicted retardance map from the model. The borders of laser writing is indicated with black lines in (c) and (f).

on non-modified regions, the model also correctly predicts the retardance in modified regions. This is possibly due to the fact that retardance in laser-written areas is affected by the stress induced by their surrounding medium. These results indicate that our analytical estimates can be used to predict the retardance map of laser-written patterns in Si, without any need for extensive simulations, which is a significant advance.

The second consideration, *i.e.*, introducing novel optical functionality, may be satisfied by fabricating laser-written wave plates inside Si. Thus, we worked on a multi-level architecture to accumulate the high retardance required for wave plates ($\pi/2$ for QWP and π for HWP). Towards this goal, an unprocessed area is sandwiched and compressed between two distinct multilevel arrays (Fig. 3(a)). The geometry of the active area (birefringent unmodified region) is designed as 2×1.2 mm^2 over the x–y plane. To keep the laser-written volume and thus fabrication time to a minimum, we used pulse energy of 2 μJ creating 5 μm structures with 5 μm separation (along the x axis). Circular polarization is used for writing, and the fabrication parameters are systematically changed to tune the retardance over the active area. The effect of two architectural parameters is evaluated, *i.e.*, the total thickness along the x dimension and the number of levels or sheets along the z dimension (Fig. 3(a)).

We first use our model to predict the induced retardance based on the thickness of single-level patterning. In order to fix the free parameter (β in Eq. (8)), we performed a calibration experiment, where an active area is created from a pair of 250 μm-thick single-level patterns. This design is replicated computationally, and the ratio between the experimental retardance and the raw value from the model is used as the scaling parameter, β. Different thicknesses are modelled (500 μm, 750 μm, and 1000 μm) using this scaling parameter and are shown with the dark blue dashed curve in Fig. 3(b). The corresponding measurements at 1058 nm wavelength are given with the red data set in Fig. 3(b). We achieve 1.26 rad of retardance with 1-mm-thick single-level writing, which corresponds to 80 MPa stress (Supplement 1, section 5). The retardance maps from the experiment and model are shown for the 750 μm-thickness case in Figs. 3(c) and 3(d), respectively. The similarity between the predicted and experimental retardance maps again indicates our high qualitative and quantitative prediction capability.

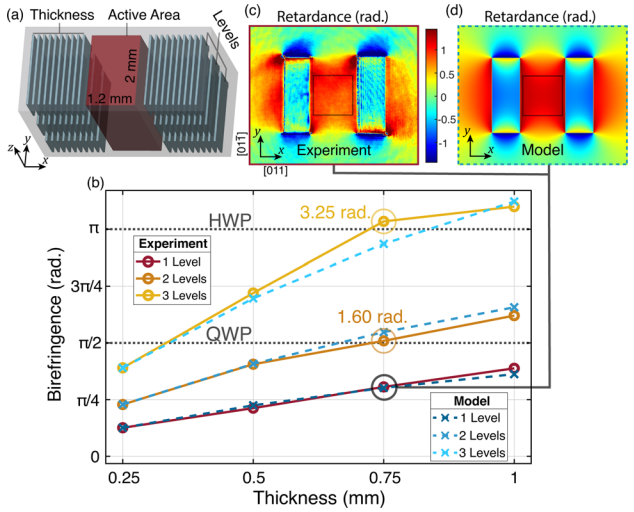

Fig. 3. (a) Architectural design for the wave plates. (b) Retardance is averaged over 1×1 mm^2 of the active area and is shown for different thicknesses and number of levels. The experimental results are shown with empty circles, and the analytical model predictions are given with crosses. The model is calibrated with the 0.25-mm-thick experimental data points. The retardance values close to HWP and QWP operation are encircled at 3.25 rad and 1.60 rad. The experimental retardance map for the 0.75-mm-thick, single-level data, and the corresponding model prediction are given in (c) and (d), respectively. The averaged 1×1 mm^2 area is indicated in (c) and (d) with black squares. Color bar applies to both (c) and (d).

Next, we aim to increase the retardance for a given thickness value and inquire the effect of multiple subsurface levels, as suggested in Fig. 3(a). Individual levels have a length of 100 μm and are written with 150 μm center-to-center distance, along the z axis. We performed experiments evaluating the retardance with increasing levels. The results are plotted in Fig. 3(b) with orange- and yellow-colored data sets for two- and three-levels; along with corresponding analytical predictions. The calibration for β in multilevel systems is performed with the 250 μm-thickness data for each level. We find that QWP operation is almost exactly attained ($\pi/2 + 0.03$, 1.9 % difference) with two levels and 750 μm thickness. HWP operation is also achieved ($\pi + 0.11$, 3.5 % difference) exploiting three levels with 750 μm thickness (Fig. 3(b)). We note that these correspond to the first polarization-control optics created inside Si.

The clear-aperture design is ideal as there is no light scattering within the active area. It has the added advantage that any fabrication imperfections in the modified regions do not directly affect the operation. Further, our tests confirmed HWP operation at the 1310 nm wavelength, indicating that the operation window may be further increased (see Supplement 1, section 4). A potential limitation of the model may arise from effects that could potentially be observed in larger-volume modifications (*e.g.*, failure of the plane strain model). We anticipate that stress engineering can help advance the accuracy of the design and introduce additional polarization control into the wafer.

We move on to the verification of HWPs as plug-and-play free-space optical elements. The sample is placed between a commercial HWP and a polarizer (Fig. 4(a)). Two sets of data are recorded at 1058 nm, one with pristine Si sample and the other with the laser-written HWP of 3.25 rad retardance (3 level,

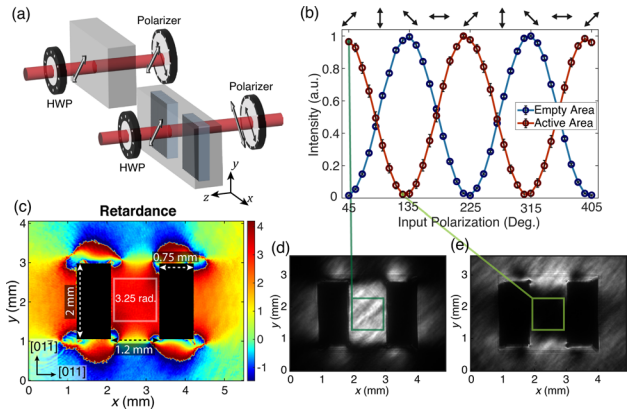

Fig. 4. (a) HWP characterization scheme based on Malus's law. (b) Transmitted intensity as a function of input polarization passing through the active region is compared with control experiment. (c) Phase difference between these curves defines the retardance, found as 3.23 rad. This is in strong agreement with phase microscopy results (3.25 rad) acquired from the retardance map. (d) and (e) Intensity images for maximum and minimum transmissions, respectively. Data in (b) are averages over the 1×1 mm^2 active area, indicated with green squares in (d) and (e).

0.75 mm thickness). The polarization state of the linearly polarized input light is controlled with the rotation of HWP, with 10° increments. The polarizer is set to pass only diagonal polarization (135° from $+x$ axis). The transmitted intensity is averaged over 1×1 mm^2 area and is plotted in Fig. 4(b). To eliminate the effects of inhomogeneity of the input beam, curves for every pixel are normalized based on the maximum value in Fig. 4(b). Since pristine Si is not birefringent, the transmitted light preserves its polarization. Thus, light is completely blocked for 45° input polarization and completely passes through for 135° polarization (Fig. 4(b), blue curve). Further, the expected sinusoidal behavior from the Malus's law is reproduced [20]. In contrast the behavior is transformed when the light passes through the fabricated HWP. The light is now completely blocked at 135° and transmits fully at 45° (Fig. 4(b), red curve). This indicates that the phase difference between blue and red curves is around π, where the active area acts as a second HWP, as expected. The phase difference between the curves in Fig. 4(b) corresponds to the retardance value of the active area. This value is computationally found from Fourier analysis as 3.23 rad and is in strong agreement with the 3.25 rad acquired from phase microscopy (Fig. 4(c)). We also show the maximum and minimum transmittance images in Figs. 4(d) and 4(e), respectively, along with the averaged active area. This set of observations reflects the uniformity and performance of laser-written subsurface HWPs.

In summary, we developed a general framework for polarization control in Si. We achieved this by modelling laser-written structures with the pressurized hole model and formulating a transfer function that can be used to predict general stress-induced retardance maps. The method is based on FFT-based operations, rapidly and accurately predicting the retardance of complex patterns. Further, we applied the approach to design and experimentally confirm laser-written patterns of high retardance (HWP, 3.25 rad). Then, 3D nonlinear laser lithography facilitated achieving the necessary stress. These optical elements constitute the first wave plates inside Si.

Funding. Türkiye Bilimler Akademisi (GEBIP); Türkiye Bilimsel ve Teknolojik Araştırma Kurumu (121F387).

Disclosures. The authors declare no conflicts of interest.

Data availability. Data can be obtained from the authors upon reasonable request.

Supplemental document. See Supplement 1 for supporting content.

REFERENCES

1. A. H. Dorrah, N. A. Rubin, A. Zaidi, M. Tamagnone, and F. Capasso, Nat. Photonics **15**, 287 (2021).
2. Q. Hu, K. Chen, J. Zhao, S. Dong, T. Jiang, and Y. Feng, Laser Photonics Rev. **17**, 2200479 (2023).
3. S. Wang, Z.-L. Deng, Y. Wang, Q. Zhou, X. Wang, Y. Cao, B.-O. Guan, S. Xiao, and X. Li, Light: Sci. Appl. **10**, 24 (2021).
4. O. Tokel, A. Turnali, G. Makey, P. Elahi, T. Çolakoglu, E. Ergeçen, Ö. Yavuz, R. Hübner, M. Zolfaghari Borra, I. Pavlov, A. Bek, R. Turan, D. K. Kesim, S. Tozburun, S. Ilday, and F. Ömer Ilday, Nat. Photonics **11**, 639 (2017).
5. X. Porte, N. U. Dinc, J. Moughames, G. Panusa, C. Juliano, M. Kadic, C. Moser, D. Brunner, and D. Psaltis, Optica **8**, 1281 (2021).
6. R. R. Gattass and E. Mazur, Nat. Photonics **2**, 219 (2008).
7. H. Zhang, S. M. Eaton, and P. R. Herman, Opt. Lett. **32**, 2559 (2007).
8. M. Ams, G. D. Marshall, P. Dekker, J. A. Piper, and M. J. Withford, Laser Photonics Rev. **3**, 535 (2009).
9. M. Sakakura, Y. Lei, L. Wang, Y.-H. Yu, and P. G. Kazansky, Light: Sci. Appl. **9**, 15 (2020).
10. B. McMillen, C. Athanasiou, and Y. Bellouard, Opt. Express **24**, 27239 (2016).
11. J. Tian, H. Yao, M. Cavillon, E. Garcia-Caurel, R. Ossikovski, M. Stchakovsky, C. Eypert, B. Poumellec, and M. Lancry, Micromachines **11**, 131 (2020).
12. A. H. Nejadmalayeri, P. R. Herman, J. Burghoff, M. Will, S. Nolte, and A. Tünnermann, Opt. Lett. **30**, 964 (2005).
13. M. Chanal, V. E. Fedorov, M. Chambonneau, R. Clady, S. Tzortzakis, and D. Grojo, Nat. Commun. **8**, 1 (2017).
14. M. Chambonneau, D. Grojo, O. Tokel, F. Ömer Ilday, S. Tzortzakis, and S. Nolte, Laser Photonics Rev. **15**, 2100140 (2021).
15. A. Turnali, M. Han, and O. Tokel, J. Opt. Soc. Am. B **36**, 966 (2019).
16. M. Schmid and H. Giessen, Opt. Lett. **47**, 5789 (2022).
17. Y. Bellouard, A. Champion, B. McMillen, S. Mukherjee, R. R. Thomson, C. Pépin, P. Gillet, and Y. Cheng, Optica **3**, 1285 (2016).
18. P. S. Theocaris and E. Gdoutos, *Matrix Theory of Photoelasticity* (Springer, 2013).
19. M. H. Sadd, *Elasticity: Theory, Applications, and Numerics* (Academic Press, 2021).
20. E. Hecht, *Optics, Global Edition* (Pearson Education, 2017).